



Cite this: *RSC Adv.*, 2024, **14**, 19718

# Polycaprolactone-MXene coating for controlling initial biodegradation of magnesium implant *via* near-infrared light†

Chen Ma,<sup>ab</sup> Hao An,<sup>a</sup> Yu-Kyoung Kim,<sup>a</sup> Seo-Young Kim,<sup>a</sup> Yong-Seok Jang <sup>\*a</sup> and Min-Ho Lee<sup>\*a</sup>

The mechanical strength of magnesium implants undergoes a rapid decline after implantation due to bioabsorption, which can lead to the risk of rupture. To ensure sustained mechanical strength and initiate bioabsorption selectively upon specific external stimuli until the bone regains sufficient support, we developed a biosafe near-infrared light (NIR)-sensitive polymer coating using polycaprolactone (PCL) and Ti<sub>3</sub>C<sub>2</sub> (MXenes). The synthetic MXene powders were characterized using SEM, EDS, and XRD, and the amount of MXenes had a proliferation-promoting effect on MC3T3-E1, as observed through cell assays. The PCL-MXene coating was successfully prepared on the magnesium surface using the casting coating method, and it can protect the magnesium surface for up to 28 days by decreasing the corrosion ratio. However, the coating can be easily degraded after exposure to NIR light for 20 minutes to expose the magnesium substrate, especially in a liquid environment. Meanwhile, the magnesium implant with the PCL-MXene coating has no cytotoxicity toward MC3T3-E1. These findings can provide a new solution for the development of controlled degradation implants.

Received 31st January 2024

Accepted 20th May 2024

DOI: 10.1039/d4ra00799a

rsc.li/rsc-advances

## 1. Introduction

Implants have received extensive research attention in the medical field and have a wide range of clinical applications, such as orthopedic implants for replacing damaged joints;<sup>1</sup> stabilizing fractures,<sup>2</sup> which aid in the healing of broken bones; dental implants for replacing missing teeth,<sup>3</sup> providing a stable foundation for dental prosthetics and providing additional support for tooth movement (temporary anchorage devices);<sup>4</sup> and organ transplants, such as heart, liver, kidney, and lung transplants. The concept of medical implants has ancient roots, with evidence of dental implants and prosthetics dating back centuries. In modern medicine, recently, implants of various materials have been rapidly developed in the bone regeneration field, such as the development of MOF coating on titanium implants to promote osteoporotic bone regeneration,<sup>5</sup> synthetic ceramic implants for bone regeneration of cranial defects,<sup>6</sup> and the investigation of highly porous, resorbable polycaprolactone scaffolds for the regeneration of large volume alveolar bone defects.<sup>7</sup> Magnesium (Mg) has become a popular metallic

implant material for bone regeneration in recent years owing to its unique properties, such as biodegradability, biocompatibility, similar mechanical properties to the bone, and promotion of bone healing;<sup>8,9</sup> however, some drawbacks such as rapid degradation, corrosion and hydrogen gas formation, are detrimental to surrounding tissues, which limit the development of Mg implants. Several treatment methods have been applied to Mg implants to overcome the inherent shortcomings of Mg, such as surface coating,<sup>10</sup> plasma electrolytic oxidation (PEO),<sup>11</sup> anodization, microarc oxidation (MAO),<sup>12</sup> surface alloying,<sup>13</sup> surface modification with organic materials,<sup>14</sup> and hybrid surface treatment.<sup>15</sup> Among them, the surface coating method has been widely studied in recent years. For example, PCL/HA hybrid coating on Mg-based alloys significantly enhanced hardness, adhesion strength, resistance to degradation and corrosion, bioactivity, and biocompatibility of the implant;<sup>16</sup> the deposition of zein/45S5 bioactive glass coating significantly improved corrosion resistance and developed hydroxyapatite crystals on the surface of the Mg substrate;<sup>17</sup> and a PCL/bioactive glass coating on Mg alloy was synthesized through electrospinning, and it reduced the degradation rate of Mg alloy by two orders of magnitude, enhanced the *in vitro* bioactivity, and revealed better adhesion and viability of cells.<sup>18</sup> Although many studies have achieved significant reductions in Mg or Mg alloy base substrate corrosion and degradation and excellent biocompatibility, it is not possible to assess the patient's recovery time with great precision before surgery due to the individual differences in preparing an implant with a matching degradation time to avoid

<sup>a</sup>Department of Dental Biomaterials, Institute of Biodegradable Materials, School of Dentistry, Jeonbuk National University, Jeon-Ju 54896, Republic of Korea. E-mail: yjang@jbnu.ac.kr; mh@jbnu.ac.kr

<sup>b</sup>School of Stomatology, Shandong First Medical University, Jinan 250117, Shandong, China

† Electronic supplementary information (ESI) available. See DOI: <https://doi.org/10.1039/d4ra00799a>



a second surgery. Therefore, the development of an Mg implant coating that can control degradation by *in vitro* stimulation is a very promising therapeutic option.

MXenes are a family of two-dimensional (2D) transition metal carbides and nitrides; among these,  $\text{Ti}_3\text{C}_2$  stands out as a prominent member, exhibiting remarkable properties, such as excellent electrical conductivity, higher surface area, good mechanical strength, and photothermal ability (NIR light). Therefore, MXene has gained significant attention in the field of energy storage devices, catalysis, sensors, and composite materials. However, MXene is still in its infancy as an implant coating material. PCL is a biodegradable and biocompatible polyester that has been widely used in various applications. With its unique combination of properties, PCL has become a valuable component of coating materials, offering advantages in terms of biodegradation, toxicity, and processing. It is worth noting that PCL degrades when the temperature is above its melting point, especially in the presence of water. Therefore, we prepare the coating material with MXene and PCL (PCL-MXene) on the Mg substrate to ensure that the synthesized coating on Mg could be degraded under *in vitro* NIR stimuli.

## 2. Materials and methods

### 2.1 Materials

Titanium aluminum carbide 312 ( $\text{Ti}_3\text{AlC}_2$ ) and polycaprolactone (Mn 80 000) were purchased from Sigma-Aldrich (St. Louis, MO, USA). Dichloromethane (methylene chloride), hydrofluoric acid, and dimethyl sulfoxide were obtained from SHOWA Chemical Co., Ltd (Tokyo, Japan). Commercially pure Mg (99.9%, Goodfellow Cambridge Limited, United Kingdom) used in this study was cut into samples of size 15 mm  $\times$  15 mm  $\times$  2 mm, and the surface of each sample was ground using #400–#2000 SIC sandpaper and washed with ethanol.

### 2.2 Synthesis and characterization of $\text{Ti}_3\text{C}_2$ MXene

A total of 0.5 g of  $\text{Ti}_3\text{AlC}_2$  powders were gradually placed in 5 mL of etchant (20% HF) and stirred with a Teflon magnetic bar for 12 hours at room temperature. After etching, the powders were washed several times with deionized water *via* centrifugation for 10 minutes (3500 RPM) until the pH of the supernatant became  $\sim$ 6. Then, 3.75 mL dimethyl sulfoxide (DMSO) was added into the etched  $\text{Ti}_3\text{C}_2$  nanosheets and stirred for 24 hours, followed by the treatment of sonication for 8 hours. The final MXene powders were obtained by lyophilization after washing with deionized water to remove extra DMSO (Fig. 1B), sealed, and stored at 4  $^\circ\text{C}$  until use.

The structure and morphology of  $\text{Ti}_3\text{AlC}_2$  and the etched MXene powder were determined using variable pressure scanning electron microscopy with energy dispersive spectroscopy (SU3900, Hitachi, Japan). The phases of  $\text{Ti}_3\text{AlC}_2$  and MXene were examined using an X-ray diffractometer (X'PERT-PRO Powder, Panalytical, UK).

### 2.3 Preparation of the PCL and PCL-MXene coatings

The PCL-MXene coating was prepared by a commonly used casting method using dichloromethane (DCM). 2% PCL was

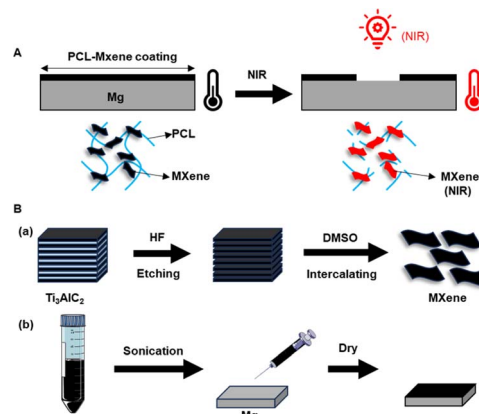


Fig. 1 (A) Degradation of the process of PCL-MXene coating on Mg under NIR light irradiation. (B) Schematic of the preparation of (a) MXenes and (b) PCL-MXene coating.

totally dissolved in DCM, followed by dispersing 12.5 mg  $\text{mL}^{-1}$  MXene powders<sup>19</sup> into the casting solution through stirring and sonication. Then, 225  $\mu\text{L}$  PCL-MXene casting solution was injected onto the surface of the Mg substrate. Finally, the samples were dried at 37  $^\circ\text{C}$  overnight, and a pure PCL coating without MXene was prepared using the same method. The bare Mg was prepared as a control group. The bare Mg, PCL, and PCL-MXene coating on Mg with NIR exposure by MDL-III-808-1 W coupled with PSU-III-LED laser power supply for 20 minutes in saline were denoted as Mg (NIR), PCL (NIR) and PCL-MXene (NIR), respectively.

### 2.4 Characterization of samples with different coatings

Fourier-transform infrared (FTIR) spectroscopy (Spectrum GX, PerkinElmer, Waltham, MA, USA) was performed at the Center for University-wide Research Facilities (CURF) of Jeonbuk National University to determine the differences in chemical bonding properties between different samples.

The thickness of the PCL-MXene coating (cross-section) and the effect of NIR exposure on the morphology of different samples were determined by variable pressure scanning electron microscopy (SU3900, Hitachi, Japan).

The infrared imaging device (FLIR Cx-Series) was used to measure and record the photothermal performance of the samples exposed to an 808 nm NIR laser. The samples were placed in 24-well plates filled with 1 mL saline and irradiated with an 808 nm NIR laser for 20 minutes. Infrared thermal images were captured by the imaging device every 5 minutes.

Differential scanning calorimetry (DSC) analyses were conducted on the samples using WATERS (Discovery SDT 650, TA Instruments) with sample masses of 6.2 mg, over a temperature range of 10–120  $^\circ\text{C}$ .

### 2.5 Electrochemical corrosion test of the PCL-MXene coating

The potentiostat/galvanostat (AMETEK PARSTAT 2273) was used to assess the anti-corrosion performance of samples in



saline at room temperature, maintaining a stable open circuit potential. A three-electrode device was used: the working electrode comprised the sample, with the Ag/AgCl/saturated KCl electrode and platinum gauze electrode serving as the reference and counter electrodes, respectively. The working electrode had an exposed area of 0.2 cm<sup>2</sup>. For electrochemical impedance spectroscopy (EIS) analysis, a sinusoidal potential of 5 mV was applied over a frequency range from 10<sup>-2</sup> Hz to 10<sup>5</sup> Hz. Potentiodynamic polarization curves were obtained at a sweep rate of 2 mV s<sup>-1</sup>. To enhance statistical robustness, each test was replicated using three parallel samples. Data analysis was performed using PowerSuite 2.55 software.

## 2.6 Immersion test of the PCL-MXene coating

The specimens, including Mg, PCL-MXene, and PCL-MXene (NIR), underwent a 28 days immersion in saline at 37 °C to assess their long-term degradation characteristics. Throughout this period, the surface morphology of the samples was examined at intervals of 0, 1, 3, 7, 14, and 28 days using a stereomicroscope (LEICA EZ4E, LEICA Microsystems, Wetzlar, Germany).

## 2.7 Cytotoxicity of the PCL-MXene coating

The cell culture medium was prepared by adding 10% fetal bovine serum (FBS, Gibco Co., USA), 500 U mL<sup>-1</sup> streptomycin (Gibco Co. USA), and 500 unit per mL penicillin (Gibco Co., USA) to  $\alpha$ -minimal essential media (MEM, Gibco, Carlsbad, CA, USA). Different concentrations of MXene and samples of cell culture extraction were prepared according to ISO 10993-12 by the immersion of powder or sample (12.5 mg mL<sup>-1</sup>) in a cell culture medium for 24 hours. Then, 1 × 10<sup>4</sup> MC3T3-E1 cells were seeded into a 96-well cell culture plate, and the cell culture medium was changed to cell culture extraction after 24 hours. The cells were cultured with a normal culture medium as a control group. After 1 and 3 days in culture, cell proliferation was determined using a CCK-8 (Enzo Life Sciences Inc., NY, USA) assay. Briefly, the cell culture medium was removed, and a fresh medium with 10% CCK-8 reagent was added. After that, the cells were further cultured at 37 °C in the incubator for 1.5 h. The formazan dye intensity was measured using an ELISA reader (Molecular Devices, EMax, San Jose, CA, USA) at a wavelength of 450 nm.

## 2.8 Statistical analysis

One-way analysis of variance (ANOVA) with a 95% confidence interval was performed to evaluate statistical significance. All analyses were performed using GraphPad Prism 8.0.2 (GraphPad Software, La Jolla, CA, USA).

# 3. Results and discussion

## 3.1 Characteristics of near-infrared light stimuli

Several stimuli such as PH, redox, glucose, light, temperature, electricity, ultrasound, and enzymes can produce structural or morphological changes in polymer materials,<sup>20</sup> and this idea has led researchers to develop some smart materials; for example, copolymers synthesized by pluronic and di-(ethylene

glycol) divinyl ether showed preferential degradation at acid PH, and it holds great potential as a pH-sensitive controlled drug delivery system.<sup>21</sup> A protective coating was constructed by hybrid polycaprolactone and indocyanine green on Mg alloys, and the degradation rate of the coating was controlled by 808 nm NIR light irradiation. These findings will provide a new strategy for designing novel photo-responsive coatings,<sup>22</sup> and a previous study reported that the mechanically triggered ring-opening of a bicyclooctene mechanophore sets up a delayed, force-free cascade lactonization that results in chain scission, which offers a strategy for enhancing mechanical degradation.<sup>23</sup> However, because the implants prepared in this study were used for *in vivo* bone regeneration, many external stimuli were not applicable; for example, heat and PH could damage the surrounding tissues, electric and magnetic fields are complicated to operate, and mechanical stimuli are not conducive to the repair of tissues, so NIR light was chosen for this study. NIR light refers to electromagnetic radiation with wavelengths ranging from 700 to 2500 nanometers; this range allows for deeper penetration into biological tissues compared to shorter wavelengths, making it suitable for imaging and therapeutic applications within the body.<sup>24</sup> NIR is generally considered safe for biological tissues and is less likely to cause phototoxic effects because it has lower energy compared to ionizing radiation, such as X-rays.<sup>25</sup> Additionally, the NIR is easy to operate without the need for invasive procedures.

## 3.2 Characterization of MXene

In the SEM images, the Ti<sub>3</sub>AlC<sub>2</sub> powders exhibit a compact layer-by-layer morphology, as illustrated in Fig. 2a. Notably, this microstructure reveals the emergence of layered flakes amidst the dense structure. Fig. 2b illustrates the disappearance of the Al layer in the Ti<sub>3</sub>AlC<sub>2</sub> particles. MXene is a photothermal material attributed to its layered structure, which offers large interlayer spacing and high surface area, providing many sites for photon absorption and efficient heat generation. The layered nature also allows for easy exfoliation into thin sheets, and the average diameter of MXene decreases significantly after DMSO treatment (Fig. 2c, and S1†), which increases the exposed surface area<sup>26</sup> and makes it distribute more uniformly in the solution, thus preparing a homogeneous PCL-MXene coating (Fig. 5). Many kinds of solutions are used to etch Ti<sub>3</sub>AlC<sub>2</sub> to obtain MXene, such as HF acid,<sup>27</sup> NH<sub>4</sub>HF<sub>2</sub>,<sup>28</sup> and LiF/HCl mixture.<sup>29</sup> MXene was successfully prepared in this study using 20% HF. It can be observed in the EDS results that the Al element is almost no longer detectable in the MXene after the Ti<sub>3</sub>AlC<sub>2</sub> is etched by HF (Fig. 2d, e and Table 1). In the XRD patterns (Fig. 3a), it can be observed that both the (002) and (004) peaks of Ti<sub>3</sub>C<sub>2</sub> MXene are moved to lower angles, the intensity of the correlation peaks become weaker and peak widths at half height become larger after being etched by HF acid, and the strong characteristic peak at 39° in 2 $\theta$  significantly decreases (PDF#97-018-2475). The findings in the XRD and EDS confirm the removal of the Al phase in Ti<sub>3</sub>AlC<sub>2</sub>.

The cytotoxicity assay conducted on MXene against MC3T3-E1 is shown in Fig. 3b. When the MXene concentration is



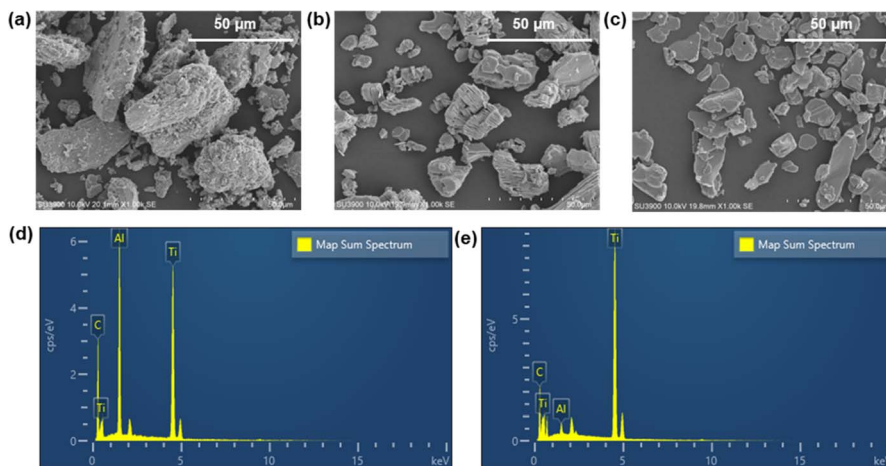


Fig. 2 SEM images of raw  $\text{Ti}_3\text{AlC}_2$  (a) and MXenes before (b) and after (c) DMSO treatment. EDS analysis of raw  $\text{Ti}_3\text{AlC}_2$  (d) and synthesized MXenes (e).

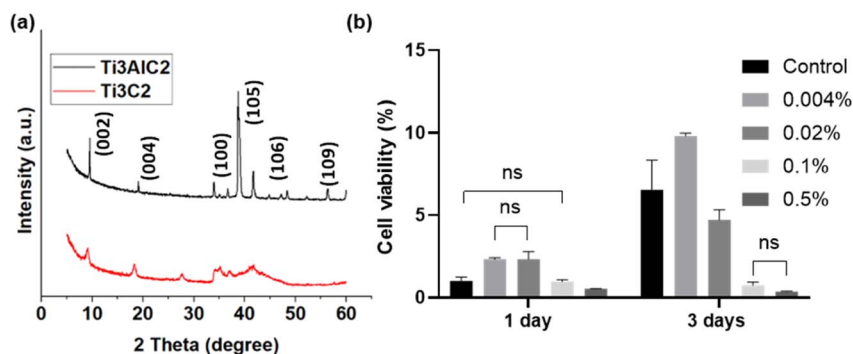


Fig. 3 (a) XRD patterns of raw  $\text{Ti}_3\text{AlC}_2$  and synthesized MXenes. (b) Cytotoxicity of different concentrations of MXenes against MC3T3-E1 using WST assay (ns,  $p > 0.05$ ).

maintained below 0.1% w/v for one day, no obvious toxicity is observed, and cell proliferation is enhanced when the concentrations of MXene are at 0.004% and 0.02% w/v. This suggests a potentially favorable cellular response to low concentrations of MXene within the initial 24 hours period. However, after 3 days, the proliferation ability of the cells was significantly inhibited when the MXene concentration was over 0.02% w/v. The cytotoxicity assessment of MXene on MC3T3-E1 cells revealed a time-dependent impact on cell activity, contingent upon the administered dosage; this phenomenon has been reported in previous studies.<sup>30</sup>

Table 1 Element weight percent from EDS

Element	$\text{Ti}_3\text{AlC}_2$ (%)	Mxene (%)
C	53.74	35.68
Al	11.66	1.08
Ti	34.59	63.24
Total	100.00	100.00
Ti/C	0.64	1.77

### 3.3 Characterization of pure PCL and PCL-MXene coating on Mg

In the FTIR spectrum, the peaks observed at  $2942\text{ cm}^{-1}$  and  $2865\text{ cm}^{-1}$  are attributed to  $\text{CH}_2$  asymmetric and symmetric stretching, while the peaks at  $1721\text{ cm}^{-1}$  and  $1160\text{ cm}^{-1}$  signify  $\text{C}=\text{O}$  and  $\text{C}-\text{C}$  stretching vibrations, respectively,<sup>31</sup> indicating that coatings containing PCL were successfully coated on the Mg surface (Fig. 4). The morphology SEM images of different samples before and after NIR light irradiation are shown in Fig. 5A. There is no difference in morphology between Mg and PCL-coated Mg before and after NIR light irradiation. However, a distinct transformation is evident in the PCL-MXene coating group. When the samples were irradiated with near-infrared (NIR) light in a saline solution for 20 minutes, the Mg substrate was exposed. Therefore, we conducted a more detailed morphology analysis on this group after NIR light irradiation (Fig. 5B). The thickness of the PCL-MXene coating on the Mg substrate was remarkably uniform and flat, measuring approximately  $13.9\text{ }\mu\text{m}$ , and it played a pivotal role in its facile degradation when exposed to NIR irradiation. This figure provides a visual representation of the consistent and well-distributed properties of the PCL-MXene layer on the



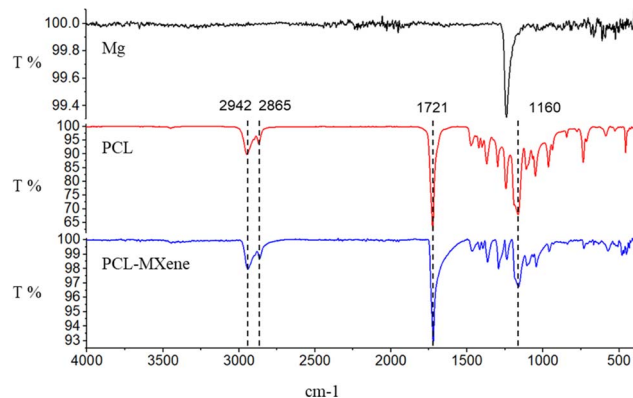


Fig. 4 FTIR spectra of Mg, PCL, and PCL-MXenes.

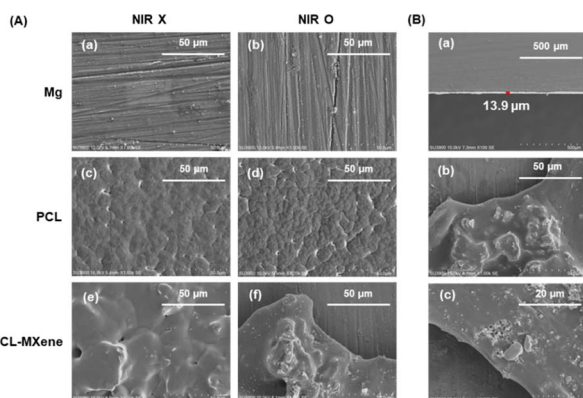


Fig. 5 (A) Comparison in SEM images between pure Mg (a and b), PCL (c and d) coating, and PCL-Mxene coating (e and f) before and after NIR light irradiation. (B) Characterization of PCL-MXene coating on Mg after irradiation with NIR light.

magnesium surface. Furthermore, it can be observed that after NIR light irradiation, in addition to significant degradation in the irradiated area, smaller degradation pores were also found around the margin. The remarkable degradability of the PCL-MXene coating under NIR irradiation can be attributed to two key factors. First, the inherent excellent photothermal ability of MXene played a crucial role. The MXene component of the coating, known for its exceptional ability to convert light into heat, facilitated the efficient absorption of NIR radiation, leading to a localized temperature increase.<sup>32</sup> The data in Fig. 6

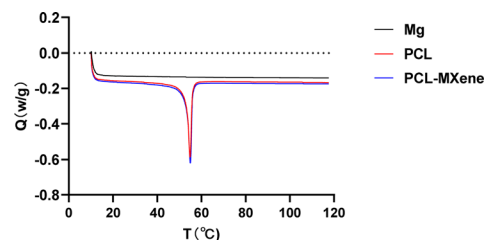


Fig. 7 DSC curves of Mg, PCL, and PCL-MXenes recorded in the 10–120 °C temperature range.

confirmed this, as the temperature of the samples prepared with MXene reached 50 °C (the actual temperature was greater than the detection temperature because the sample was taken out for measurement) after 20 minutes of NIR light irradiation, which was much higher than the other groups. Second, degradability was also influenced by the intrinsic ability of PCL to undergo degradation in liquid environments when subjected to temperatures exceeding its relatively low melting point (50–70 °C).<sup>30,33</sup> Our DSC experiments obtained similar results, and the melting point of the coating in the PCL and PCL-MXene groups was 55 °C (Fig. 7). The combination of MXene's photothermal prowess and PCL's temperature-sensitive degradation characteristics in liquid environments synergistically contributed to the controlled and efficient disintegration of the coating under NIR irradiation.

Based on the aforementioned experimental results, the pure PCL coating did not undergo degradation upon NIR irradiation. Therefore, we excluded this group from the following experiments.

### 3.4 Controlled anticorrosion properties of PCL-MXene coating

The protective efficacy of the PCL-MXene coating on Mg substrates and the impact of NIR irradiation on the coating's integrity were systematically assessed through electrochemical corrosion analysis, encompassing potentiodynamic polarization and EIS (Fig. 8). The corrosion potential was evaluated by the abscissa of the intersection point, and the current density from the intersection of the Tafel extrapolation. The measured corrosion potential ( $E_{\text{corr}}$ ) and corrosion current density ( $i_{\text{corr}}$ ) for Mg, Mg (NIR), PCL-MXene, and PCL-MXene (NIR) are listed in Table 2. The corrosion current density is a direct indicator of

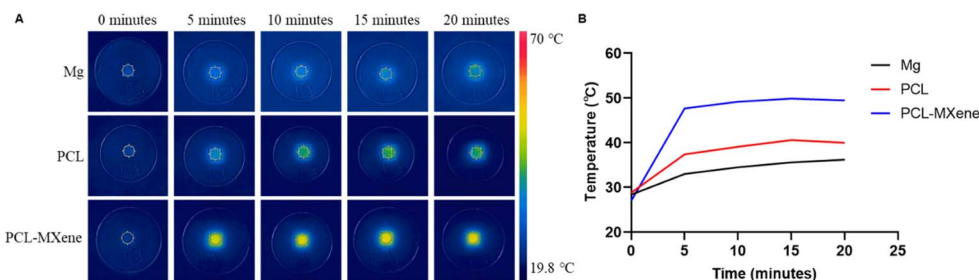


Fig. 6 Real-time infrared thermal images (A) and photothermal heating curves (B) of different samples immersed in NaCl under continuous 808 nm laser irradiation for 20 minutes.

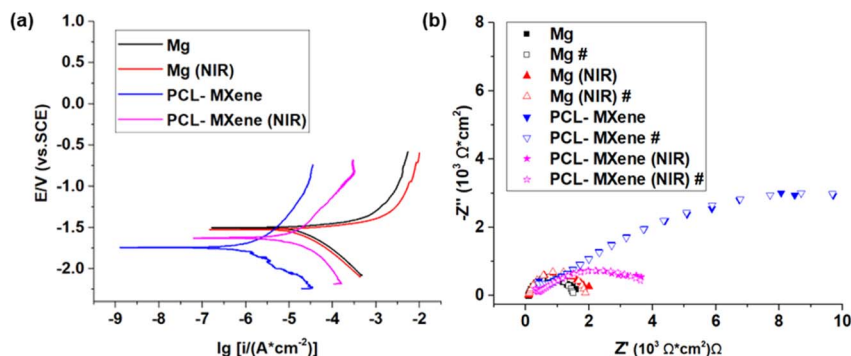


Fig. 8 Electrochemical corrosion analysis of the effect of NIR on bare Mg and PCL-MXene coating on Mg, (a) potentiodynamic polarization measurement of each group and (b) raw data and fitting results (#) of each group Nyquist plots.

Table 2 Results of corrosion potentials,  $E_{\text{corr}}$ , and corrosion current densities,  $i_{\text{corr}}$

	$E_{\text{corr}}$ (V <sub>SCE</sub> )	$i_{\text{corr}}$ (A cm <sup>-2</sup> )
Mg	$-1.53 \pm 0.01$	$(3.43 \pm 0.08) \times 10^{-2}$
Mg (NIR)	$-1.53 \pm 0.02$	$(2.99 \pm 0.15) \times 10^{-2}$
PCL-MXene	$-1.73 \pm 0.04$	$(1.74 \pm 0.08) \times 10^{-3}$
PCL-MXene (NIR)	$-1.65 \pm 0.11$	$(2.14 \pm 0.07) \times 10^{-2}$

sample corrosion resistance. More specifically, the  $i_{\text{corr}}$  values of Mg, Mg (NIR), PCL-MXene, and PCL-MXene (NIR) were  $(3.43 \pm 0.08) \times 10^{-2}$ ,  $(2.99 \pm 0.15) \times 10^{-2}$ ,  $(1.74 \pm 0.08) \times 10^{-3}$ , and  $(2.14 \pm 0.07) \times 10^{-2}$  A cm<sup>-2</sup>, respectively. There is no significant difference in  $i_{\text{corr}}$  of Mg before and after NIR treatment. The  $i_{\text{corr}}$  of PCL-MXene was reduced by ~20 times compared with that of the bare Mg. This significant reduction attests to the efficacy of the PCL-MXene coating in shielding the magnesium substrate, markedly enhancing the overall corrosion resistance of the sample. However, the  $i_{\text{corr}}$  of PCL-MXene (NIR) was significantly higher than the coating before NIR treatment and similar to bare Mg. This result suggests that the PCL-MXene coating undergoes accelerated degradation under the influence of NIR irradiation. The corrosion resistance of the samples was further investigated using the Nyquist plot. The Nyquist plots of Mg, Mg (NIR), PCL-MXene, and PCL-MXene (NIR) in saline solution are shown in Fig. 8b. The Mg and Mg (NIR) had a similar capacitive loop; compared with the bare Mg, the PCL-MXene showed a larger capacitive loop. However, the capacitive loop of PCL-MXene (NIR) significantly decreased after NIR treatment. The resistances calculated from each Nyquist plot were fitted numerically using the equivalent circuits presented in Fig. 9. The fitting results are shown in Table 3, where  $R_s$  is the solution resistance,  $R_c$  is the resistance of the oxide layer in the bare Mg samples,  $R_t$  is the resistance of the coating in the coating samples,  $R_i$  is the charge transfer resistance, and  $\text{CPE}_c$  and  $\text{CPE}_t$  are the constant phase elements. The analysis results of the Nyquist plot further illustrate the corrosion resistance characteristics. The resistance of the PCL-MXene coating  $((4.37 \pm 1.54) \times 10^2 \Omega \text{ cm}^2)$  was significantly greater than that of the oxide layer in Mg  $((1.02 \pm 0.18) \times 10^2 \Omega \text{ cm}^2)$  and Mg (NIR)  $((8.47 \pm 1.64) \times 10^1 \Omega \text{ cm}^2)$ . However, the resistance of the PCL-MXene

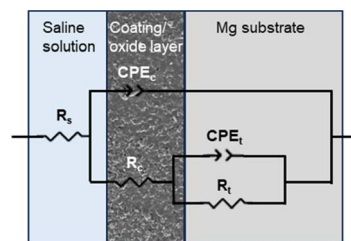


Fig. 9 Equivalent circuits for fitting Nyquist plots of Mg, Mg (NIR), PCL-MXenes, and PCL-MXene (NIR) samples.

decreased to  $(2.70 \pm 0.93) \times 10^2 \Omega \text{ cm}^2$  after NIR treatment due to the degradation of the PCL-MXene coating. The same trend is more evident in the charge transfer resistance, where Mg and Mg (NIR) have similar and small values of  $(1.71 \pm 0.41) \times 10^3 \Omega \text{ cm}^2$  and  $(1.90 \pm 0.12) \times 10^3 \Omega \text{ cm}^2$ , respectively. After the PCL-MXene layer is prepared, the value increases significantly to  $(1.77 \pm 0.12) \times 10^4 \Omega \text{ cm}^2$ . However, the value decreases to  $(4.73 \pm 0.41) \times 10^3 \Omega \text{ cm}^2$  after NIR irradiation. The charge transfer resistance is a valid parameter for confirming the protective properties of coatings. It increased approximately 10 times in the PCL-MXene groups compared to that in the bare Mg group and significantly decreased after NIR irritation. The distinct trends in both corrosion current density and the Nyquist plot analysis results collectively underscore the protective attributes of the PCL-MXene coating and its susceptibility to NIR-induced degradation.

### 3.5 Stability of PCL-MXene coating

The stability of implant materials is a pivotal criterion for assessment,<sup>34</sup> and the immersion test is a common method for studying the long-term stability of materials. The microscopy images of Mg, PCL-MXene, and PCL-MXene (NIR) after immersion in the saline are shown in Fig. 10. The surface color of the bare Mg group began to change after 1 day of immersion in saline and became grayish white after 28 days, which was attributed to the oxidation, corrosion, and degradation of the bare Mg in saline. No significant changes in the surface coating of the PCL-MXene group were detected after 28 days of immersion in saline. This absence of change indicates that the



Table 3 Fitting results of the Nyquist plots using an equivalent circuit shown in Fig. 7

	$R_s$ ( $\Omega$ cm <sup>2</sup> )	$CPE_c$		$CPE_c$		$N$	$R_t$ ( $\Omega$ cm <sup>2</sup> )
		$Y_0$ (S sec <sup><i>n</i></sup> )	$N$	$Y_0$ (S sec <sup><i>n</i></sup> )	$N$		
Mg	$(3.76 \pm 3.51) \times 10^{-2}$	$(3.79 \pm 0.19) \times 10^{-9}$	1	$(1.02 \pm 0.18) \times 10^2$	$(2.79 \pm 0.04) \times 10^{-5}$	$(8.34 \pm 0.11) \times 10^{-1}$	$(1.71 \pm 0.41) \times 10^3$
Mg (NIR)	$(1.83 \pm 1.18) \times 10^{-2}$	$(3.81 \pm 0.25) \times 10^{-9}$	1	$(8.47 \pm 1.64) \times 10^1$	$(2.57 \pm 0.04) \times 10^{-5}$	$(8.38 \pm 0.03) \times 10^{-1}$	$(1.90 \pm 0.12) \times 10^3$
PCL-MXene	$(3.27 \pm 0.38) \times 10^{-5}$	$(1.78 \pm 0.32) \times 10^{-9}$	1	$(4.37 \pm 1.54) \times 10^2$	$(1.49 \pm 0.05) \times 10^{-5}$	$(4.61 \pm 0.32) \times 10^{-1}$	$(1.77 \pm 0.12) \times 10^4$
PCL-MXene (NIR)	$(8.42 \pm 0.17) \times 10^{-3}$	$(1.79 \pm 0.08) \times 10^{-9}$	1	$(2.70 \pm 0.93) \times 10^2$	$(4.11 \pm 0.85) \times 10^{-5}$	$(4.52 \pm 0.27) \times 10^{-1}$	$(4.73 \pm 0.41) \times 10^3$

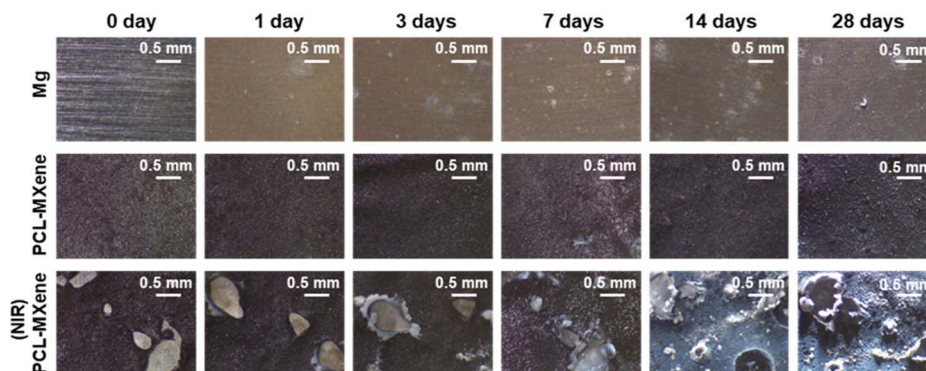
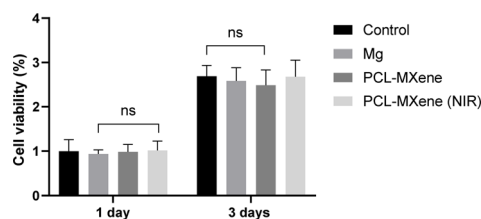


Fig. 10 Microscopy images of each group sample after immersion test in saline for 28 days.

Fig. 11 Cell viability of each group against MC3T3-E1 after 1 and 3 days (ns,  $p > 0.05$ ).

PCL-MXene coating provides prolonged protection to the underlying Mg substrate. However, upon exposure to NIR irradiation, the coating exhibited a distinct response in the PCL-MXene (NIR) group. After 20 minutes of NIR irradiation, the coating was defective and the substrate magnesium was exposed; however, the defects due to PCL degradation did not increase significantly with the increase in immersion time upon 28 days. Despite this, the corrosion and degradation of the Mg substrate occurred, which are attributed to the penetration of the saline solution through the defects that came into direct contact with the Mg substrate. Importantly, the results obtained from the degradation experiments align closely with the experimental objectives of this study, shedding light on the interplay between the protective attributes of the PCL-MXene coating and its responsiveness to external stimuli.

### 3.6 Cytotoxicity of PCL-MXene coating

Achieving good biocompatibility is a fundamental requirement for implanted biomaterials to effectively fulfill their intended functions within the human body. The cytotoxicity of PCL-

MXene coating Mg samples before and after NIR irradiation was investigated by WST assay, as shown in Fig. 11. There were no significant differences observed among all groups at either the 1 day or 3 days cell culture period, underscoring the biocompatible nature of the PCL-MXene coating, both in the normal state and under the influence of NIR irradiation. These results are particularly promising in the context of biomedical applications.

## 4. Conclusions

A biosafe stimulus-sensitive polymer coating on Mg using MXene and PCL was developed in this study. The structure and cytotoxicity of synthesized MXene were investigated. A super thin coating was fabricated using the casting method, exhibiting the capacity to protect the Mg surface for up to 28 days by decreasing the corrosion rate. Furthermore, this coating can undergo controlled degradation under NIR light exposure for 20 minutes, revealing the underlying Mg substrate. These findings offer a viable solution for enhancing the longevity and controlled degradation of Mg-based implants, presenting a promising avenue for biomedical applications.

## Author contributions

Conceptualization, C. M., Y.-K. K., S.-Y. K., Y.-S. J., and M.-H. L.; performed experiments, C. M.; analyzed data, C. M. and Y.-S. J.; writing—original draft preparation, C. M.; writing—review and editing, C. M., Y.-K. K., S.-Y. K., Y.-S. J., and M.-H. L. (all authors had final input); visualization, C. M.; supervision, Y.-K. K., S.-Y.



K., Y.-S. J., and M.-H. L.; project administration, Y.-K. K., Y.-S. J., and M.-H. L.; funding acquisition, S.-Y. K., and M.-H. L.

## Conflicts of interest

There are no conflicts to declare.

## Acknowledgements

This research was supported by the “National Research Foundation of Korea (NRF) grant funded by the Korea government (MSIT) (No. 2021R1A2C2005466 and No. 2021R1C1C2006915)”.

## Notes and references

- 1 M. Z. Ibrahim, A. A. D. Sarhan, T. Y. Kuo, F. Yusof, M. Hamdi and T. M. Lee, *Surf. Coat. Technol.*, 2020, **392**, 125755.
- 2 S. Lang, C. Neumann, C. Schwaiger, A. Voss, V. Alt, M. Loibl and M. Kerschbaum, *BMC Musculoskeletal Disord.*, 2021, **22**, 1–13.
- 3 J. Z. Niu, Y. H. Guo, K. Li, W. J. Liu, Z. H. Dan, Z. G. Sun, H. Chang and L. Zhou, *Mater. Sci. Eng., C*, 2021, 122.
- 4 M. Giri, K. Sabapathy, B. Govindasamy and H. Rajamurugan, *J. World Fed. Orthod.*, 2020, **9**, 13–17.
- 5 M. W. Chen, D. Wang, M. H. Li, Y. He, T. T. He, M. H. Chen, Y. Hu, Z. Luo and K. Y. Cai, *ACS Nano*, 2022, **16**(9), 15397–15412.
- 6 O. Omar, T. Engstrand, L. K. B. Linder, J. Åberg, F. A. Shah, A. Palmquist, U. Birgersson, I. Elgali, M. Pujari-Palmer, H. Engqvist and P. Thomsen, *Proc. Natl. Acad. Sci. U. S. A.*, 2020, **117**, 26660–26671.
- 7 M. Bartnikowski, C. Vaquette and S. Ivanovski, *Clin. Oral Implants Res.*, 2020, **31**, 431–441.
- 8 P. Rider, Z. P. Kacarevic, A. Elad, D. Tadic, D. Rothamel, G. Sauer, F. Bornert, P. Windisch, D. B. Hangyási, B. Molnar, E. Bortel, B. Hesse and F. Witte, *Bioact. Mater.*, 2022, **14**, 152–168.
- 9 Z. P. Kacarevic, P. Rider, A. Elad, D. Tadic, D. Rothamel, G. Sauer, F. Bornert, P. Windisch, D. B. Hangyási, B. Molnar, T. Kämmerer, B. Hesse, E. Bortel, M. Bartosch and F. Witte, *Bioact. Mater.*, 2022, **14**, 15–30.
- 10 Y. W. Zhu, W. Liu and T. Ngai, *J. Polym. Sci.*, 2022, **60**, 32–51.
- 11 C. Rendenbach, H. Fischer, A. Kopp, K. Schmidt-Bleek, H. Kreiker, S. Stumpp, M. Thiele, G. Duda, H. Hanken, B. Beck-Broichsitter, O. Jung, N. Kröger, R. Smeets and M. Heiland, *Mater. Sci. Eng., C*, 2021, **129**, 112380.
- 12 R. F. Zhang, S. Zhong, L. L. Zeng, H. Y. Li, R. F. Zhao, S. F. Zhang, X. T. Duan, J. S. Huang and Y. Zhao, *Materials*, 2021, **14**(19), 5710.
- 13 M. Rahman, N. K. Dutta and N. R. Choudhury, *Front. Bioeng. Biotechnol.*, 2020, **8**, 564.
- 14 S. A. Rahim, M. A. Joseph, T. S. S. Kumar and H. Hanas, *Front. Mater.*, 2022, **9**, 848980.
- 15 A. S. Gnedenkov, V. S. Filonina, S. L. Sinebryukhov and S. V. Gnedenkov, *Molecules*, 2023, **28**(6), 2538.
- 16 M. Rahman, M. A. Chowdhury, M. S. Mia, M. R. Ali, A. Rahman, M. O. Ali and S. Mahmud, *Ceram. Int.*, 2022, **48**, 23314–23324.
- 17 M. A. U. Rehman, *Prosthesis*, 2020, **2**, 211–224.
- 18 Z. Panahi, E. Tamjid and M. Rezaei, *Surf. Coat. Technol.*, 2020, **386**, 125461.
- 19 L. Liu, B. Huang, X. Liu, W. Yuan, Y. Zheng, Z. Li, K. W. K. Yeung, S. Zhu, Y. Liang and Z. Cui, *Bioact. Mater.*, 2021, **6**, 568–578.
- 20 X. L. Hu, Y. G. Zhang, Z. G. Xie, X. B. Jing, A. Bellotti and Z. Gu, *Biomacromolecules*, 2017, **18**, 649–673.
- 21 V. K. Garripelli, J. K. Kim, R. Namgung, W. J. Kim, M. A. Repka and S. Jo, *Acta Biomater.*, 2010, **6**, 477–485.
- 22 Z. X. Han, X. M. Liu, L. Tan, Z. Y. Li, Y. F. Zheng, K. W. K. Yeung, Z. D. Cui, Y. Q. Liang, S. L. Zhu and S. L. Wu, *Rare Met.*, 2021, **40**, 2538–2551.
- 23 Y. J. Lin, T. B. Kouznetsova, C. C. Chang and S. L. Craig, *Nat. Commun.*, 2020, **11**(1), 4987.
- 24 X. Xiong, Z. Xu, H. B. Huang, Y. Wang, J. Y. Zhao, X. Guo and S. B. Zhou, *Biomaterials*, 2020, **245**, 119840.
- 25 B. Pucelik, A. Sulek and J. M. Dabrowski, *Coord. Chem. Rev.*, 2020, 416.
- 26 L. Jin, X. Q. Guo, D. Gao, C. Wu, B. Hu, G. X. Tan, N. N. Du, X. L. Cai, Z. Yang and X. C. Zhang, *NPG Asia Mater.*, 2021, **13**(1), 24.
- 27 M. Naguib, M. Kurtoglu, V. Presser, J. Lu, J. J. Niu, M. Heon, L. Hultman, Y. Gogotsi and M. W. Barsoum, *Adv. Mater.*, 2011, **23**, 4248–4253.
- 28 M. Ghidui, M. Naguib, C. Shi, O. Mashtalir, L. M. Pan, B. Zhang, J. Yang, Y. Gogotsi, S. J. L. Billinge and M. W. Barsoum, *Chem. Commun.*, 2014, **50**, 9517–9520.
- 29 M. Ghidui, M. R. Lukatskaya, M. Q. Zhao, Y. Gogotsi and M. W. Barsoum, *Nature*, 2014, **516**, 78–U171.
- 30 S. H. Lee, S. Jeon, X. Qu, M. S. Kang, J. H. Lee, D. W. Han and S. W. Hong, *Nano Convergence*, 2022, **9**(1), 38.
- 31 C. Chen, F. Liu, X. Zhang, Z. Zhao and S. J. Liu, *Beilstein J. Org. Chem.*, 2019, **15**, 992–999.
- 32 D. X. Xu, Z. D. Li, L. S. Li and J. Wang, *Adv. Funct. Mater.*, 2020, **30**(47), 2000712.
- 33 A. Fernández-Tena, R. A. Pérez-Camargo, O. Coulembier, L. Sangroniz, N. Aranburu, G. Guerrica-Echevarria, G. Liu, D. Wang, D. Cavallo and A. J. Müller, *Macromolecules*, 2023, **56**, 4602–4620.
- 34 A. L. Foster, T. F. Moriarty, C. Zalavras, M. Morgenstern, A. Jaiprakash, R. Crawford, M. A. Burch, W. Boot, K. Tetsworth, T. Miclau, P. Ochsner, M. A. Schuetz, R. G. Richards and W. J. Metsemakers, *Injury*, 2021, **52**, 43–52.

